

**Maximizing wind farm power output with the helix approach  
Experimental validation and wake analysis using tomographic particle image velocimetry**

van der Hoek, Daan; den Abbeele, Bert Van; Simao Ferreira, Carlos; van Wingerden, Jan Willem

**DOI**

[10.1002/we.2896](https://doi.org/10.1002/we.2896)

**Publication date**

2024

**Document Version**

Final published version

**Published in**

Wind Energy

**Citation (APA)**

van der Hoek, D., den Abbeele, B. V., Simao Ferreira, C., & van Wingerden, J. W. (2024). Maximizing wind farm power output with the helix approach: Experimental validation and wake analysis using tomographic particle image velocimetry. *Wind Energy*. <https://doi.org/10.1002/we.2896>

**Important note**

To cite this publication, please use the final published version (if applicable).  
Please check the document version above.

**Copyright**

Other than for strictly personal use, it is not permitted to download, forward or distribute the text or part of it, without the consent of the author(s) and/or copyright holder(s), unless the work is under an open content license such as Creative Commons.



**Takedown policy**

Please contact us and provide details if you believe this document breaches copyrights.  
We will remove access to the work immediately and investigate your claim.

## RESEARCH ARTICLE

WILEY

# Maximizing wind farm power output with the helix approach: Experimental validation and wake analysis using tomographic particle image velocimetry

Daan van der Hoek<sup>1</sup>  | Bert Van den Abbeele<sup>1</sup> | Carlos Simao Ferreira<sup>2</sup> | Jan-Willem van Wingerden<sup>1</sup> 

<sup>1</sup>Delft Center for Systems and Control, Faculty of Mechanical Engineering, Delft University of Technology, Delft, The Netherlands

<sup>2</sup>Department of Flow Physics and Technology, Faculty of Aerospace Engineering, Delft University of Technology, Delft, The Netherlands

## Correspondence

Daan van der Hoek, Delft Center for Systems and Control, Delft University of Technology, 2628 CD Delft, The Netherlands.  
[d.c.vanderhoek@tudelft.nl](mailto:d.c.vanderhoek@tudelft.nl)

## Funding information

This work is part of the Hollandse Kust Noord wind farm innovation program where CrossWind C.V., Shell, Eneco, and Siemens Gamesa are teaming up; funding for the PhDs was provided by CrossWind C.V. and Siemens Gamesa. This work is part of the research programme “Robust closed-loop wake steering for large densely spaced wind farms” with project number 17512, which is (partly) financed by the Dutch Research Council (NWO).

## Abstract

Wind farm control can play a key role in reducing the negative impact of wakes on wind turbine power production. The helix approach is a recent innovation in the field of wind farm control, which employs individual blade pitch control to induce a helical velocity profile in a wind turbine wake. This forced meandering of the wake has turned out to be very effective for the recovery of the wake, increasing the power output of downstream turbines by a significant amount. This paper presents a wind tunnel study with two scaled wind turbine models of which the upstream turbine is operated with the helix approach. We used tomographic particle image velocimetry to study the dynamic behavior of the wake under the influence of the helix excitation. The measured flow fields confirm the wake recovery capabilities of the helix approach compared with normal operation. Additional emphasis is put on the effect of the helix approach on the breakdown of blade tip vortices, a process that plays an important role in re-energizing the wake. Measurements indicate that the breakdown of tip vortices and the resulting destabilization of the wake are enhanced significantly with the helix approach. Finally, turbine measurements show that the helix approach was able to increase the combined power for this particular two-turbine setup by as much as 15%.

## KEYWORDS

dynamic individual pitch control, experimental validation, the helix approach, tomographic piv, wind farm control, wind farm power maximization

## 1 | INTRODUCTION

Wakes generated by upstream turbines can negatively impact the performance of downstream turbines and the wind farm as a whole. They contribute to significant losses in energy and increased loading of structural components.<sup>1,2</sup> While conventional industry practice takes these negative aspects for granted, there are ways to, at least partially, mitigate wake effects. Wind farm control can play a key role in reducing wake effects by actively influencing the airflow behind turbines. Three wind farm control categories are generally recognized.<sup>3–5</sup> *Axial induction control* (AIC) adjusts the induction factor of the turbine either by introducing an offset in the blade pitch angle or running the turbine at a sub-optimal tip speed

This is an open access article under the terms of the [Creative Commons Attribution-NonCommercial](https://creativecommons.org/licenses/by-nc/4.0/) License, which permits use, distribution and reproduction in any medium, provided the original work is properly cited and is not used for commercial purposes.

© 2024 The Authors. *Wind Energy* published by John Wiley & Sons Ltd.

ratio.<sup>5,6</sup> While AIC has proven capable of providing grid services<sup>7-9</sup> and decreasing structural loading,<sup>10,11</sup> applying it for maximizing power has seen less convincing results.<sup>12-15</sup> The second category is called *wake steering* and has been shown numerous times to be capable of increasing the power output of wind turbine arrays. By misaligning upstream turbines with respect to the incoming wind and redirecting the wake away from downstream turbines, the latter are able to extract more power and more than overcome the losses incurred by the yaw misalignment.<sup>13,16-22</sup> The last 5 years has seen an increasing interest in the third category, which is often referred to as *dynamic induction control* (DIC) or *wake mixing*. Methods belonging to this category make continuous adjustments to the turbines' operating setpoints to increase the level of mixing in the wake and thereby enhance its dissipation. In this paper, we will also focus on a method from this category.

DIC was first applied in large eddy simulations through dynamic variations of a wind turbine's induction factor and showed large increases in power output.<sup>23,24</sup> A simplified implementation of this concept was introduced by Munters and Meyers<sup>25</sup>, consisting of a periodic variation in thrust which only depends on an optimal amplitude and frequency. Frederik et al<sup>15</sup> tested this method in the wind tunnel on a three-turbine array by feeding a sinusoidal pitch reference signal to the upstream turbine. Depending on the frequency and, more importantly, the amplitude of the pitch reference, power gains in the range of 2% were observed. Several studies on the wake recovery mechanism of DIC were made using both simulations<sup>26-28</sup> and wind tunnel experiments.<sup>29</sup> These studies all showed that dynamic thrust adjustments affect the pairing behavior of subsequent blade tip vortices, a process that is closely associated with re-energizing the wake.<sup>30</sup> When active, DIC accelerates the vortex pairing, creating a region of high vorticity around which the surrounding flow rolls up. Subsequently, higher energy flow is entrained into the wake.

An extension of the previous method was presented by Frederik et al.<sup>31</sup>, where they used dynamic individual pitch control (DIPC) to induce periodic yaw and tilt moments on the rotor plane. Due to the imposed phase difference in yaw and tilt moments, the location of the thrust force varies periodically around the center of the rotor plane with a near-constant radius. This leads to a helical structure in the velocity profile of the wake, for which this technique was dubbed the *helix approach*. By periodically pitching the blades at a slightly lower or higher frequency than the rotor frequency, a clockwise (CW) or counter-clockwise (CCW) helix shape is created. Large eddy simulations with both uniform and turbulent inflow showed that this type of actuation can be very successful in enhancing wake mixing and was able to increase the power output of a two-turbine array up to 7.5%.

The helix approach was further explored with large eddy simulations in terms of finding the optimal excitation frequency<sup>32</sup> and amplitude.<sup>33,34</sup> The optimal frequency, usually expressed by the dimensionless Strouhal number (St), was found to be higher compared with DIC with collective pitch actuation. As for the optimal amplitude, Taschner et al<sup>34</sup> detected no saturation in the power gain in low turbulence conditions for pitch amplitudes of up to 6°, indicating that the power gains will primarily be limited by the level of turbulence and the allowed increase in structural loading caused by the helix approach. Korb et al<sup>35</sup> used large eddy simulations to investigate the wake of a single turbine and concluded that the helix approach is responsible for both increased mixing and significant wake deflection. Furthermore, simulations with three turbines demonstrated how phase differences between the helical wakes can have a significant impact on the power performance. Aero-elastic simulations have indicated significant increases in the fatigue loading of both blades and tower of the actuated turbine with the helix approach, although not as significant as in the case of DIC.<sup>34,36,37</sup> The loads of the downstream turbine were also seen to increase by a small amount but not comparable with the actuated turbine.

Previous work on the helix approach all agrees that the technique is most efficient in the CCW direction when considering power maximization. A similar comparison between the two helix counterparts was also made by Coquelet<sup>38</sup>, who simulated the performance of the helix approach using a vortex-particle-mesh code. These simulations once more showed the superiority of the CCW helix over the CW version. However, the simulation results also indicated that the potential power gain of the helix decreases significantly as the resolution of the simulations increases. This suggests that previously reported gains obtained through large eddy simulations might be largely overestimated, and in the case of the CW, helix might not even be present.

The work from Coquelet<sup>38</sup> highlights the importance of validating wind farm control methods in real-life scenarios, starting with wind tunnel experiments and followed by field testing. This standpoint is reinforced by experts in both academia and industry, who rank a lack of validation as the primary barrier to implementing wind farm control methods on commercial wind farms.<sup>3</sup> A first step in the validation of the helix approach was taken by Heckmeier<sup>39</sup>, who successfully implemented it in the wind tunnel on a two-turbine array. A multihole pressure probe was used to measure the velocity profile of a horizontal slice of the wake, indicating increased wake recovery. While these measurements allowed for a phase-locked representation of the wake based on the azimuthal position of the blades, the true transient behavior of the helix approach was not observed.

In this paper, we present an experimental investigation of the helix approach implemented on a scaled wind turbine model. Individual pitch control can be problematic for small-scale turbines, both due to limited space for actuators as well as higher pitch rates. To overcome this challenge, the turbine was equipped with a swashplate that enables cyclic pitch adjustments. We further expand upon the experiments carried out by Heckmeier<sup>39</sup>. Using a similar two-wind turbine setup, a full three-dimensional, quasi-time-resolved characterization of the wake is obtained using particle image velocimetry (PIV). The quasi-time-resolved nature of the measurement results was obtained by phase averaging the PIV data based on both the rotor azimuth angle and the phase of the helix approach. This approach differs from the work of Heckmeier<sup>39</sup>, which only considered phase averaged measurements based on rotor azimuth angle, thereby obscuring the tip vortex interaction at different phases of the helix excitation. Similar to previous experimental studies that incorporated PIV to investigate tip vortex interaction and the entrainment of kinetic energy into

the wake (e.g.,<sup>40–42</sup>), we will investigate how the helix method affects these aspects. This paper will contribute in a major way to the existing literature in two ways. First, the work is seen as another important validation of the helix approach using an alternative turbine model and in a different wind tunnel. A contribution that will hopefully help pave the way to future field testing. Second, the PIV measurements allow for an extensive analysis of the dynamic behavior in the wake as a result of the helix approach, shedding more light on its working principles.

## 2 | EXPERIMENT SETUP

### 2.1 | Wind turbine model

For this experiment, we used two MoWiTO-0.6 wind turbines developed by the University of Oldenburg.<sup>43</sup> The turbine has a rotor diameter of  $D = 0.58\text{m}$ . The rotor speed can be controlled by regulating the generator torque. The standard turbine model is equipped with a single stepper motor that pitches the blades collectively. To achieve the necessary individual pitch action required for replicating the helix approach, some adjustments to the turbine were made. Due to the dimensions of the turbine, using three motors to drive each pitch bearing directly was not a feasible option. The solution was to implement a swashplate mechanism that is commonly used in helicopters.

A visualization of the swashplate design is given in Figure 1. The swashplate consists of a non-rotating part that is actuated by three stepper motors driving three control rods along threaded shafts. The rotating component of the swashplate is connected to the blade mounting mechanism using three pitch links. Both swashplate components are fitted on the rotor shaft using spherical bearings, allowing sufficient range of motion. By tilting the lower swashplate to an arbitrary position, the upper swashplate is forced to assume the same position, which in turn leads to a different pitch setting for each of the three blades. When the rotor is spinning, this will automatically result in a sinusoidal adjustment of the pitch angle of each blade over a single revolution.

The deformation of the tower in the fore-aft direction was measured using a set of strain gauges applied to the bottom of the tower. The strain gauges were connected in a full Wheatstone bridge configuration, with strain expressed as a single voltage measurement. Prior to testing, the strain gauges were calibrated to obtain an expression of the bending moment at the tower base as a function of voltage.

The control inputs for the stepper motors and generator torque were sent through a *dSPACE MicroLabBox* real-time system, which was also connected to a computer. A *SIMULINK* model used for operating the wind turbine was compiled on the *dSPACE* system, which was called to send and receive data using a *MATLAB* script. Communication took place at a frequency of 2 kHz, where besides sending the control input signals, sensor data were acquired of the stepper motor encoders, generator current, generator speed, rotor azimuth position, and tower bottom strain. At the start of the experimental campaign, the optimal operating conditions were determined empirically for both turbines. The power coefficient was determined using the measured generator current, which was multiplied by a generator-specific torque constant and the rotor speed to obtain electrical power.<sup>43</sup> The power coefficient was seen reaching its maximum value of  $C_{P_e} \approx 0.27$  with a blade pitch angle of  $\theta = 10^\circ$  and tip-speed ratio of  $\lambda = \Omega R / U_\infty = 5$ . Here,  $\Omega$  refers to the rotor speed,  $R$  the rotor radius, and  $U_\infty$  the free stream inflow velocity. The definition of the pitch angle is based on assigning a  $0^\circ$  pitch angle to the most outward position the blades could be pitched to (i.e., pitched fully into the incoming flow). The generator torque of both turbines was regulated in two different ways. For the upstream turbine, we wanted to avoid any effect a varying rotor speed could have on the thrust force. Hence, a straightforward proportional-integral feedback controller was implemented to regulate

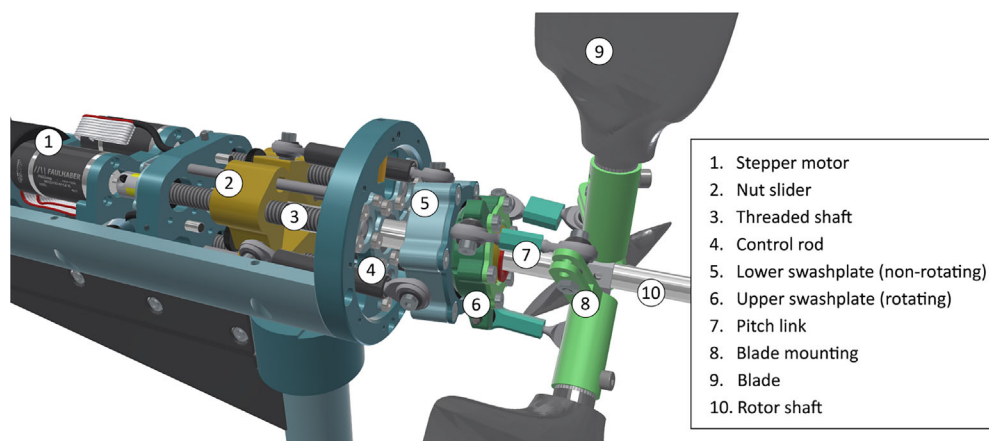


**FIGURE 1** Overview of the swashplate design listing all the involved components. The stepper motors are used to move nut sliders over a threaded shaft, which are in turn connected to the lower swashplate. The upper swashplate assumes the same orientation as the lower swashplate, resulting in different pitch angles for each blade.

the torque based on the measured rotor speed, ensuring a near-constant rotor speed, and consequently a constant  $\lambda$ , during all measurements. For the downstream turbine, the incoming flow velocity was unknown, meaning that the previous strategy could not be implemented. To optimize the power extraction for the downstream turbine, the torque was regulated based on the measured rotor speed with the  $K\Omega^2$ -control law.<sup>44</sup>

## 2.2 | Implementing the helix approach

With the adjusted turbine model presented in the previous section, actuating the turbine to recreate the helix is relatively straightforward. The original helix control strategy used the multiblade coordinate (MBC) transformation<sup>45</sup> to transform the varying tilt and yaw moments into inputs for the pitch controller. The swashplate can be viewed as a mechanical counterpart to the MBC transformation, meaning that we only have to supply the desired frequency and amplitude of the swashplate motion as inputs to our wind turbine. Since the swashplate actuators are spaced  $120^\circ$  apart, moving the swashplate periodically in a CW or CCW motion requires applying a sinusoidal reference to all stepper motors, with offsets of  $\pm 120^\circ$  and  $\pm 240^\circ$  to the second and third motors relative to the first. In this case, a positive offset results in a CW movement of the swashplate when viewing the turbine from the front. An example of the control inputs is provided on the left side of Figure 2.

An initial study into the optimal amplitude and frequency of the swashplate motion was performed prior to the PIV measurements. By varying the amplitude and frequency, and recording the combined power of the two turbines, the settings were found that resulted in optimal power extraction at a wind speed of  $U_\infty = 5 \text{ m s}^{-1}$ . The highest power gain for the CW case was found with an amplitude of  $180^\circ$  on the stepper motors, while an amplitude of  $216^\circ$  showed the largest gain for the CCW case. It has to be noted that the latter was the highest amplitude the stepper motors were able to reach at this particular wind speed, without faults being introduced in the tracking of the reference signals. The optimal excitation frequencies  $f_e$ , expressed by the Strouhal number  $St = f_e D / U_\infty$ , were determined experimentally at  $St = 0.34$  ( $f_e = 0.21f_r$ ) and  $St = 0.28$  ( $f_e = 0.18f_r$ ) for the CW and CCW helix cases, respectively. Here,  $f_r$  represents the rotational frequency of the turbine. The resulting excitation frequencies are close to the optimal frequency of  $f_e = 0.18f_r$  reported by Heckmeier<sup>39</sup>. For the PIV measurements, we therefore decided to implement both helix cases at these optimal frequencies, while using an amplitude of  $180^\circ$  for the stepper motor actuation to compare both methods. Additional measurements were also taken for a  $CCW_{opt}$  case with an amplitude of  $216^\circ$ .

Measurements of the actual blade pitch angles were taken after the experimental campaign. By fitting a potentiometer directly to each of the blade mounting mechanisms seen in Figure 1, the pitch angles were recorded for different azimuth positions and orientations of the swashplate. The evolution of the pitch angle of a single blade over time is presented on the right-hand side of Figure 2 for one amplitude of the stepper motors. This figure shows the difference in pitch rates of the two methods. As the swashplate is moving in the CW direction, similar to the rotational direction of the rotor, the blades are not able to complete a full pitch cycle over a single rotation of the rotor. The opposite is true for the CCW case, resulting in a pitch frequency that is slightly higher than the rotational frequency. Apart from the differences in pitch rate, one can also observe that for both methods the amplitude varies over time. This is the result of some compromises that were made when designing the swashplate to allow sufficient freedom of movement. The dashed lines in the figure show the ideal pitch angles based on the average amplitudes that were measured using the potentiometer. An unexpected property of the swashplate design is that for a single motor amplitude, the resulting pitch amplitudes for the CW and CCW direction are not equal (i.e., the swashplate experiences more/less freedom of movement depending on the direction it is moving). The difference in average pitch amplitude between test cases is something that should be considered when analyzing the measurement results in Section 3.

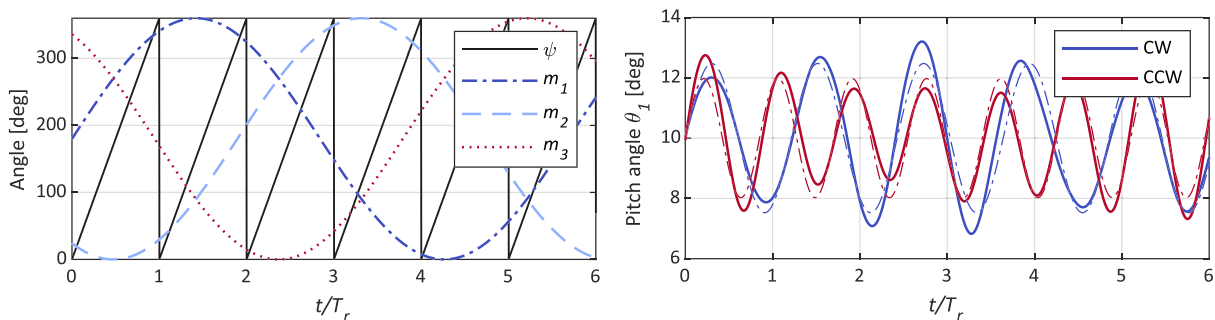


**FIGURE 2** The left figure shows an example of CW actuation of the three stepper motors ( $m_1$ ,  $m_2$ , and  $m_3$ ) used for controlling the motion of the swashplate. The black line indicates the rotor azimuth position  $\psi$ . The right figure shows a comparison between a CW and CCW motion of the swashplate and the resulting pitch angles for one of the blades. The dashed lines show the ideal pitch actuation based on the average pitch amplitude of both helix cases. In both figures, time  $t$  is normalized by the turbine rotation period  $T_r$ . CW, clockwise; CCW, counter-clockwise.

The variation of the blade pitch amplitude over time will also have an impact on the quality of the yaw and tilt moments that are being exerted on the incoming flow. We can observe the extent of this variation using the MBC transformation<sup>45</sup>

$$\begin{bmatrix} \theta_0(t) \\ \theta_{\text{tilt}}(t) \\ \theta_{\text{yaw}}(t) \end{bmatrix} = \frac{2}{3} \begin{bmatrix} 0.5 & 0.5 & 0.5 \\ \cos(\psi) & \cos\left(\psi + \frac{2}{3}\pi\right) & \cos\left(\psi + \frac{4}{3}\pi\right) \\ \sin(\psi) & \sin\left(\psi + \frac{2}{3}\pi\right) & \sin\left(\psi + \frac{4}{3}\pi\right) \end{bmatrix} \begin{bmatrix} \theta_1(t) \\ \theta_2(t) \\ \theta_3(t) \end{bmatrix}, \quad (1)$$

where  $\theta_0$ ,  $\theta_{\text{tilt}}$ , and  $\theta_{\text{yaw}}$  represent the fixed reference frame collective, tilt, and yaw angles. Figure 3 presents the transformed tilt and yaw angles for the CCW helix based on the measured pitch angles. The measured angles are compared with the ideal tilt and yaw reference angles, shown by the dashed lines, in case of a constant amplitude on the blade pitch inputs. From the figure, it is evident that the swashplate is able to move the pitch angles in such a way as to obtain a 90° offset between the tilt and yaw angles. While the tilt angle shows a good fit to the ideal reference, it seems that some imperfections in the swashplate design result in a small bias for the yaw angle. Based on this, a small warping of the helix velocity profile can be expected.

### 2.3 | Wind tunnel experiment design

The experiment was carried out at TU Delft's Open Jet Facility. The wind tunnel consists of an octagonal-shaped open jet with dimensions of 2.85 m by 2.85 m, which is run in a closed circuit. The flow is passed through a radiator system to keep the flow temperature near constant. Before exiting the jet, the flow is contracted by a 3:1 ratio, reaching velocities of up to 35 m s<sup>-1</sup> at turbulence intensities (TI) ranging between 0.5% and 2%<sup>42</sup>. During all measurements of the experimental campaign, the wind tunnel was operated at a constant velocity of  $U_\infty = 5 \text{ m s}^{-1}$ .

The two MoWiTO-0.6 turbines were placed on a large platform, set apart by a distance of 5 rotor diameters ( $D$ ), similar to other studies on the helix approach.<sup>31,39</sup> The remaining measurement equipment is illustrated in Figure 4. A seeding rake was placed at the outlet of the open jet, releasing neutrally buoyant helium-filled soap bubbles (HFSBs), with an average diameter of 0.4 mm that were used as flow tracers over an area 0.6 m wide by 0.9 m high.<sup>46</sup> On their way downstream, the flow tracers were illuminated by two *LaVision LED Flashlights*. The resulting reflections were recorded by a tomographic PIV system consisting of four *Photron FASTCAM SA1.1* high-speed cameras, operating with a framerate of 500 frames/s and at a resolution of 1024 by 1024 pixels. Each recording acquired 5000 frames, resulting in approximately 24 cycles of the helix approach. Synchronization between cameras and LEDs was arranged using a *LaVision PTU-X* timing device. The measurement domain was divided into seven smaller volumes of size  $0.4 \times 0.7 \times 0.7 \text{ m}^3$ , which were covered by moving the construction on which the cameras and LEDs were mounted. The measurement volumes overlapped in the streamwise direction ( $x$ ), resulting in a total volume of  $2.1 \times 0.7 \times 0.7 \text{ m}^3$  and covering a portion of the turbine wake ranging from 0.7–4.3  $D$ . The resulting image resolution was equal to 1.99 pixels/mm.

An overview of all the test cases that were measured is presented in Table 1. Different implementations of the helix approach were compared with a baseline case, where both turbines were operated using *greedy* control. This control strategy is standard industry practice and is referred to as *greedy*, because the turbine aims to maximize its own power production. In doing so, it disregards any impact it has on turbines operating in its wake.

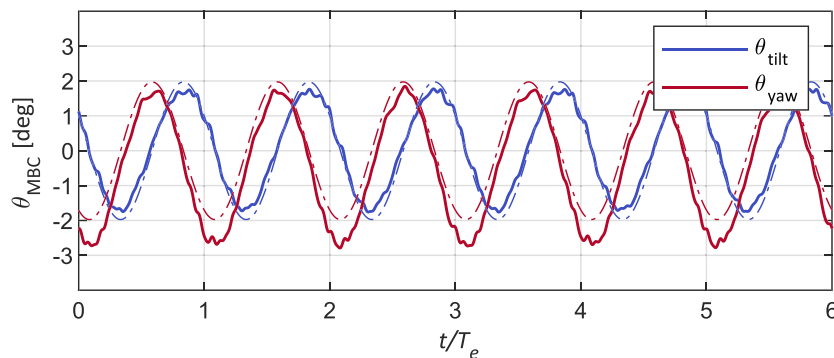


**FIGURE 3** Fixed frame tilt and yaw angles for the CCW helix implementation as a function of time normalized by the excitation period  $T_e = 1/f_e$ . The dashed lines show the ideal tilt and yaw angles, in the case of a constant amplitude of the pitch angles in the rotating reference frame. CCW, counter-clockwise.

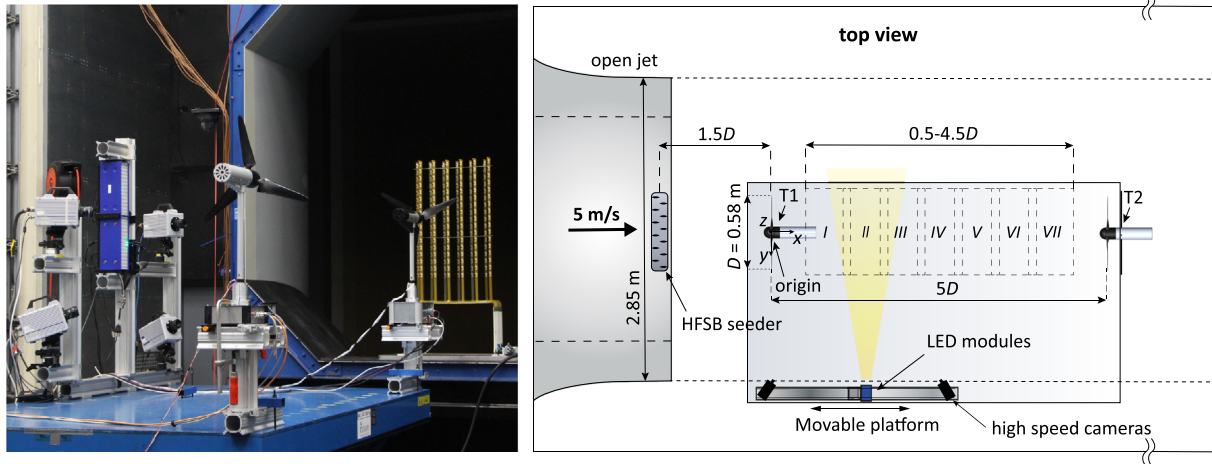


**FIGURE 4** Overview of the experimental setup, highlighting the different components and the measured sections of the wake. The field of views indicated by the numbers I–VII are centered at distances of  $1 : 0.5 : 4D$  behind the upstream wind turbine. The cameras and LEDs were mounted on a frame that could be moved along the platform accordingly.

**TABLE 1** All test cases that were considered for the PIV measurements, indicating the Strouhal number, average pitch amplitude  $A_\theta$ , the total number of frames that were recorded for each measurement volume, and the total number of helix cycles that were completed during the measurements.

Test case	Strouhal nr.	$A_\theta$	# frames	# helix cycles
Baseline (greedy)	n.a.	n.a.	10,000	n.a.
Helix CW	0.34	$2.5^\circ$	15,000	82
Helix CCW	0.28	$2.0^\circ$	15,000	72
Helix CCW <sub>opt</sub>	0.28	$2.4^\circ$	5,000	24

Abbreviations: CW, clockwise; CCW, counter-clockwise.

The PIV data were processed using *LaVision's DaVis 10* software. A high-pass filter was applied to the raw data to reduce any background illumination.<sup>47</sup> A geometrical mapping of the camera positions relative to the measurement domain was obtained using a calibration plate, followed by a volume self-calibration<sup>48</sup> to reduce the residual measurement errors below 0.1 pixels. Next, we reconstructed the flow tracers with the Shake-The-Box algorithm<sup>49</sup>, resulting in approximately 20,000 identified particle tracks per time step. The final processing step consisted of mapping the particle track data onto a Cartesian grid by spatially averaging over small cells. For this binning procedure, we used  $40 \times 40 \times 40 \text{ mm}^3$  cells with a Gaussian weighing function. An overlap of 75% was selected to obtain a grid spacing of 10 mm in the resulting velocity fields. The average number of particles used in the binning procedure for each grid point consisted of 30,000 particles for the time-averaged flow fields and around 900 particles for the phase-averaged flow fields.

The measurement setup has many similarities to the one used in van der Hoek et al.,<sup>29</sup> where we measured the effect of periodic DIC with collective pitch on a turbine wake. Some improvements that were made for the current experiment compared with the previous setup consisted of (1) A movable construction for the cameras, as opposed to moving the turbine with respect to the jet outlet, which was seen to have some impact on the turbine inflow conditions. (2) Adding a fourth camera and increasing the tomographic angle (i.e., the subtended angle of all cameras with respect to the measurement domain). This resulted in improved reconstruction of the velocity fields and an increased field of view (FOV). (3) Multiple repetitions of the same control action were recorded for improved convergence of the velocity fields. (4) The distance to the HFSB seeder was increased somewhat to reduce its impact on the inflow conditions. (5) The total length of the measurement domain was increased to capture a larger portion of the wake.

Prior to the helix experiments, we measured the flow without any turbines at a distance of  $2.5D$  downstream of the seeding rake to get an approximation of the inflow conditions at the upstream turbine (T1). The average measured wind speed and TI profiles at a hypothetical rotor plane are given in Figure 5. Both the horizontal and vertical velocity profiles are seen to be centered around the specified inflow speed of  $U_\infty = 5 \text{ m s}^{-1}$ . The TI in both directions slightly exceeded the earlier specified level of 2%, indicating only a marginal increase in turbulence at the inflow of the turbine as a result of the seeding rake. A similar influence of the seeding rake on the flow conditions was reported by Jux et al.<sup>50</sup>

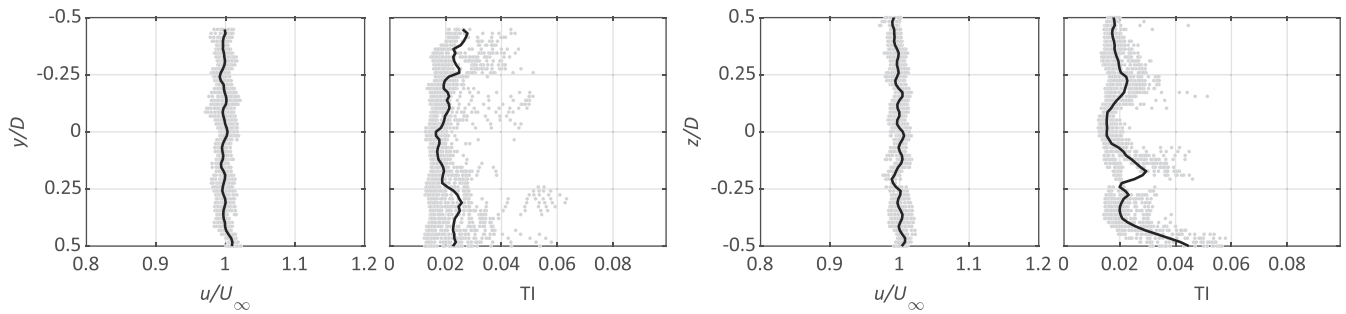


**FIGURE 5** Horizontal ( $y$ ) and vertical ( $z$ ) profiles of the inflow obtained without the presence of a turbine. The gray lines indicate the flow profiles at a single height or width, while the black lines represent the flow profiles averaged over all heights or widths. Note that not all parts of the measurement volume were seeded sufficiently with flow tracers, due to some blocked channels of the seeding rake.

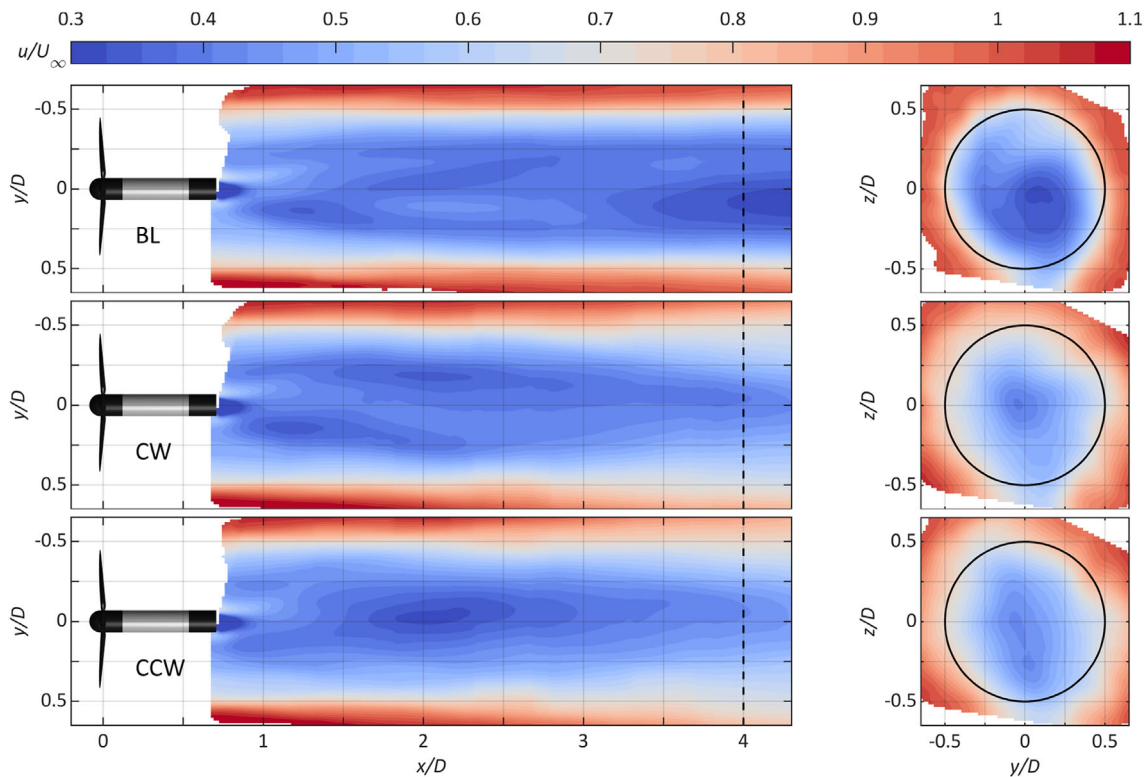


**FIGURE 6** Normalized streamwise velocity contours  $u/U_\infty$  reconstructed from the time-averaged particle data. The velocity contours at  $z/D = 0$  and  $x/D = 4$  compare baseline operation with the CW and CCW helix implementations. The dashed line indicates the location of the wake cross-section, while the black circle shows the size of the rotor. CW, clockwise; CCW, counter-clockwise.

### 3 | RESULTS

The flow fields that are presented in this section only consider the first three test cases from Table 1. The fourth test case consisting of the CCW<sub>opt</sub> helix with larger pitch amplitude had a smaller amount of measurement data, meaning that the resulting flow fields (primarily phase-averaged) are of somewhat lesser quality. For this reason, we decided to omit the flow fields in the paper and only consider this test case for some additional analysis of the power performance. Please note when comparing the remaining flow fields of the helix approach that there is a small difference in average pitch amplitude between CW and CCW actuation, making a one-on-one comparison more difficult.



### 3.1 | Time-averaged flow fields

The binning procedure described in Section 2 was initially applied to all particle data at once, providing the time-averaged flow fields. The streamwise velocity fields of the turbine operating under different control strategies are shown in Figure 6. For the baseline case, the horizontal cross-section of the turbine wake remains relatively constant. This indicates that there is little recovery in the portion of the wake that was measured. Both helix cases show a clear improvement in wake recovery, marked by a larger wake expansion, but a narrower wake deficit profile. This is most obvious from the vertical cross-section of the wake at  $x/D = 4$ . Here, we also observe some differences in the shape of the wake between the CW and CCW helix. This difference is believed to be the result of how the shape of the helix (CW or CCW) interacts with the natural rotation of the wake. Further research is needed to define how this interaction affects the shape and recovery of the wake.

An indication of the level of wake recovery or *entrainment* is given by the flux of mean kinetic energy across the shear layer of the wake. Starting from the transport equation for mean kinetic energy, Cal et al<sup>40</sup> showed that the flux of mean kinetic energy due to Reynolds shear stresses is the dominant factor for the entrainment of energy into a turbine wake. An expression for the flux of mean kinetic energy can be obtained using the triple decomposition for a velocity component  $u$ <sup>51</sup>:

$$u = \bar{u} + u', \quad (2)$$

with  $\bar{u}$  the time-averaged velocity component and  $u'$  the fluctuation of the velocity component. The latter term can be further decomposed as

$$u' = \tilde{u} + u_s, \quad (3)$$

where  $\tilde{u}$  and  $u_s$  represent periodic and stochastic fluctuations in the flow, respectively. The flux of mean kinetic energy due to shear stress in the vertical plane is subsequently given by

$$\phi = -\overline{u'w'}\bar{u}. \quad (4)$$

The term  $\overline{u'w'}$  indicates the time-averaged Reynolds shear stress in the vertical plane, which is computed as

$$\overline{u'w'} = \frac{\sum_{k=1}^N (u(t_k) - \bar{u})(w(t_k) - \bar{w})}{N}, \quad (5)$$

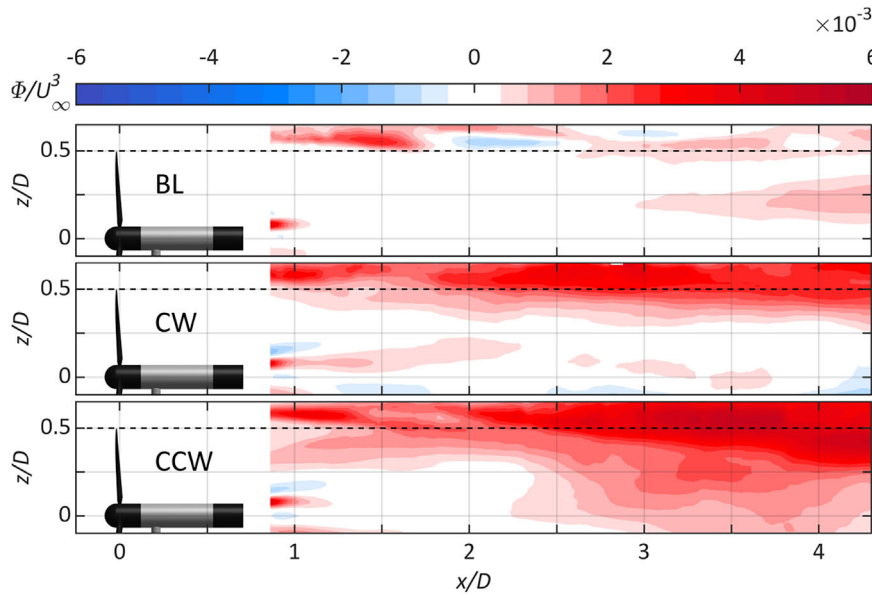


**FIGURE 7** Vertical flow field ( $y/D = 0$ ) of the normalized flux of mean kinetic energy into the wake region. Positive (red) values indicate flux of mean kinetic energy in the negative  $z$  direction (downward). We are primarily interested in the flux crossing the boundary of the wake, marked by the dashed line. The figure shows a comparison between baseline operation, CW helix, and CCW helix. CW, clockwise; CCW, counter-clockwise.

with  $u(t_k)$  and  $w(t_k)$  the in-plane velocity components at time instant  $t_k$ , for a number of samples  $N$ . Entrainment of mean kinetic energy toward the center of the wake can occur when high-speed areas outside the wake move inward ( $u' > 0$  and  $w' < 0$ ) or when low-speed areas from inside the wake are ejected outward ( $u' < 0$  and  $w' > 0$ ). Hence, positive values of the mean kinetic energy flux correspond to wake recovery.

The improved wake mixing achieved with both helix methods can be seen in Figure 7, which shows the entrainment or flux of mean kinetic energy into the region of the wake outlined by  $z/D = 0.5$ . Looking at the baseline case, we initially see little entrainment across the wake shear layer. Around a distance of  $x/D = 2$ , one can observe a clear sign flip in the flux of mean kinetic energy. The sign flip is the result of a change in relative orientation of two interacting tip vortices. This interaction is generally referred to as leapfrogging or vortex pairing. Following the completion of this leapfrogging motion, an increase in kinetic energy entrainment into the wake was seen.<sup>30</sup> Observing this phenomenon, Lignarolo et al<sup>30</sup> concluded that leapfrogging is closely related to the re-energizing of the wake and that accelerated breakdown of the tip-vortices will result in earlier and thus an increased recovery of the wake velocity.

For both helix cases, Figure 7 shows large increases in entrainment, starting earlier than the baseline case and rising even more after  $x/D = 2$ . Unlike the baseline case, we do not see a clear sign flip in the entrainment indicating the leapfrogging location. This is the combined result of a varying leapfrogging location and the forced meandering of the wake as a result of the periodic tilt and yaw moments exerted at the rotor, leading to a more diffused entrainment profile. The variation in leapfrogging location was also observed for DIC by collective blade pitch in both simulations<sup>28</sup> and a wind tunnel study.<sup>29</sup> In case of DIC, the periodic thrust variations lead to differences in the strength and expansion of the tip vortices. This increases the reciprocal influence of the helical tip vortices, triggering the mutual-inductance instability mode more aggressively.<sup>52</sup> As a result, the mixing process in the wake and the resulting re-energization becomes more effective. Similar to DIC, the helix approach alters the strength of vortices that are shed from the blades due to the varying pitch angles, inserting higher levels of instability in the resulting vortex rings. Furthermore, these variations are distributed asymmetrically over the rotor.

Figure 7 offered a glance at the magnitude of velocity fluctuations present in the wake for the different test cases. However, given the definition of the time-averaged Reynolds stress from Equation (5), it does not distinguish between periodic and random contributions toward the entrainment of energy in the wake. Lignarolo et al<sup>42</sup> showed that the net periodic contribution (e.g., from tip vortices) to the transport of energy to the wake was nearly zero. Essentially, the tip vortices shield the wake and thereby prevent mixing of the wake with the surrounding flow. Following the completion of the leapfrogging motion, positive entrainment of energy was observed, which was solely dependent on random turbulent fluctuations in the flow. Using phase-averaged PIV measurements, we can study the contribution of turbulent fluctuations to the recovery of the wake in a similar manner for the helix cases.

### 3.2 | Phase-averaged flow analysis

The PIV measurements were obtained in a time-resolved manner and would therefore be suitable for dynamic analysis by themselves were it not for the fact that the seeding of the flow tracers in the wake is not entirely uniform. As a result, fewer particles are recorded in some areas of the wake which means the measurement convergence might be lower in those parts. This problem can be overcome by phase-averaging the particle data during postprocessing. This means that for each phase, more particles are available to each bin on the Cartesian grid, leading to a higher convergence of the velocity components.

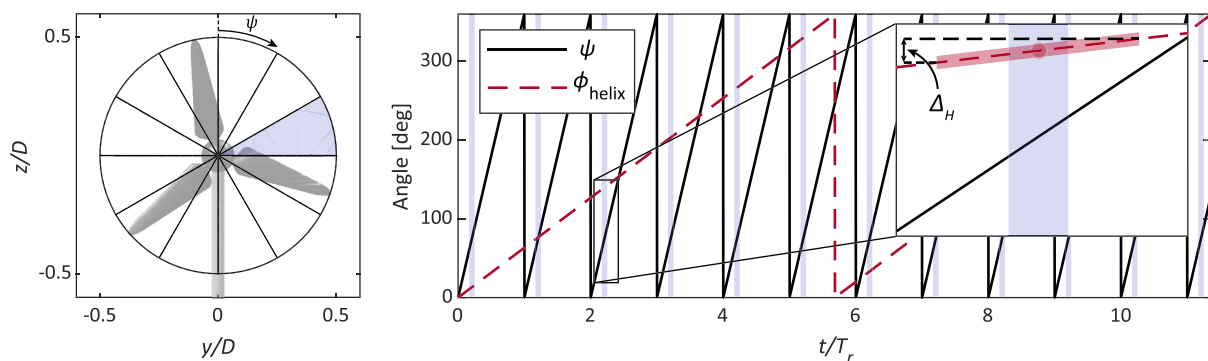


**FIGURE 8** Graphical illustration of the phase-averaging procedure in case of a CCW helix implementation. Data is initially binned based on the measurement of the rotor azimuth position  $\psi$ , with bin sizes of  $30^\circ$ . Furthermore, measurements of the helix approach are binned based on a second criterion, which is the so-called helix azimuth angle  $\phi_{\text{helix}}$ . For a particular rotor azimuth bin, indicated by the blue shaded area, the corresponding average helix azimuth bin is determined. All data that falls within  $\pm\Delta_H/2$  of this helix azimuth bin, as well as the previously defined rotor azimuth bin, is collected for phase-averaging. Note that the figure contains a schematic representation of  $\Delta_H$ , and does not correspond to the actual bin width used in the paper. The rotor and helix azimuth angles are indicated as a function of the number of rotor revolutions  $t/T_r$

For the baseline case, we phase-averaged the data using the measurement of the rotor azimuth angle  $\psi$ . The rotor was divided into twelve equal parts of  $30^\circ$ , as seen on the left side of Figure 8. Hence, the dynamics of the flow are now represented by 12 consecutive flow fields. On average, over 800 frames (i.e., sets of particle data at a specific time instant) were used for the averaging of each azimuth bin.

Phase-averaging measurement data for the helix approach is less straightforward than in the previous case. Again, the data initially need to be sorted using the rotor azimuth to retain the flow information from root and tip vortices. However, due to the individual pitch action, this only delivers the average performance of the helix over a single rotation as shown in Heckmeier.<sup>39</sup> To visualize the dynamic effects of the helix approach, we used a second binning criterion that incorporates the angle between the yaw and tilt moments from Figure 3. This angle, referred to as the helix azimuth angle, is given by

$$\phi_{\text{helix}} = \tan^{-1} \left( \frac{\theta_{\text{tilt}}}{\theta_{\text{yaw}}} \right). \quad (6)$$

The new binning procedure is visualized on the right-hand side of Figure 8, which shows the two sawtooth waves for the rotor azimuth  $\psi$  and helix azimuth  $\phi_{\text{helix}}$ . Unfortunately, the frequencies of the rotor and the two helix test cases did not match up perfectly. For each CCW cycle of the helix, the rotor completes  $f_r/f_e = 5.68$  revolutions. This means that we have to go through three helix cycles before both the rotor and helix azimuth angles return to approximately the same initial conditions. Consequently, the number of bins used for phase-averaging is expressed by  $f_r/f_e \times (\# \text{ of helix cycles}) \times (\# \text{ of azimuth bins})$ , where the number of helix cycles is chosen to obtain an integer, approximately, when multiplying with  $f_r/f_e$ . For the CW case, this resulted in 168 bins, while 204 bins were obtained for the CCW case due to the slightly lower excitation frequency.

A single rotor azimuth bin is plotted in Figure 8 for each consecutive revolution of the rotor by the light blue shaded area. Zooming in on one of these azimuth bins, we see that the range of  $\phi_{\text{helix}}$  corresponding to this bin is limited. To increase the number of samples for each bin, an additional variable is introduced representing the width of the helix azimuth bin  $\Delta_H$ . Investigating the effect of this variable on the resulting velocity fields, a bin width of  $\Delta_H = 40^\circ$  was seen to provide converged results. Summarizing the binning procedure: For each consecutive rotor azimuth bin (168 and 204 bins for the CW and CCW cases, respectively), the corresponding helix azimuth angle is determined, after which all frames that belong to this rotor azimuth angle and fall within the bin of the helix azimuth angle are collected from the full set of measurements for the averaging procedure. On average, around 150 PIV frames were used to obtain the velocity fields of each bin in the case of the helix approach. Converting these PIV frames to velocity fields was done in the same manner as for the time-averaged flow fields.

The phase-averaged velocity fields of the baseline and CW helix cases are compared in Figure 9. The wake of the turbine operating under baseline control is shown for a single azimuth bin. This velocity field is similar to its time-averaged counterpart. However, the presence of tip vortices provides some additional detail in the shear layer of the wake. The velocity fields of the CW helix are given at four different phases of the helix cycle. The top view provides a clear picture of the forced meandering caused by the varying yaw and tilt moments. The CW movement of the wake is also clearly seen through the cross-sections at  $x/D = 4$ . Figure 9 also contains isosurfaces of the  $Q$ -criterion,<sup>53</sup> which were used to reconstruct the tip vortices. The  $Q$ -criterion is a common vortex identification method that is computed using the velocity gradient matrix  $\nabla U$ <sup>54</sup>:

$$Q = \frac{1}{2} \left( \text{tr}(\nabla U)^2 - \text{tr}((\nabla U)^2) \right), \quad (7)$$

where  $\text{tr}$  represents the mathematical trace of a matrix. The  $Q$ -criterion identifies areas in the wake where the vorticity dominates the strain rate, revealing well-defined tip vortices. A clear difference is observed in the pairing of the tip vortices between the baseline and helix case. While the former shows an organized and gradual leapfrogging process, the latter is quite aggressive and results in an accelerated breakdown of the tip vortices. A detailed analysis of the tip vortex interaction is presented in Section 3.4.

The performance of the helix approach compared with baseline operation can already be quantified using the streamwise velocity fields as shown in Figure 9. The fraction of available power  $f_{\text{AP}}$  indicates the amount of power that is available compared with the free stream inflow to a hypothetical turbine in the wake.<sup>55</sup> This performance criterion is given by

$$f_{\text{AP}}(x) = \int_0^{2\pi} \int_0^R u^3(x, r, \psi) / U_\infty^3 r dr d\psi, \quad (8)$$

with  $x$  denoting the distance downstream,  $r$  the radial distance measured from the rotor center, and azimuth angle  $\psi$ . Figure 10 presents the  $f_{\text{AP}}$  for each of the different test cases from Table 1. In the figure, the CCW helix implementation with an average amplitude of  $A_\theta = 2.4^\circ$  is referred to as  $\text{CCW}_{\text{opt}}$ . All three helix implementations initially see similar levels of available power in the wake, though below baseline operation. Under baseline operation, the power decreases at a slower rate until it settles to a near-constant value around  $x/D = 2$ , showing no signs of recovery in the wake domain that was measured. The CW and CCW implementations reach their minimum level between  $x/D = 1.5$  and  $x/D = 2$ , after which

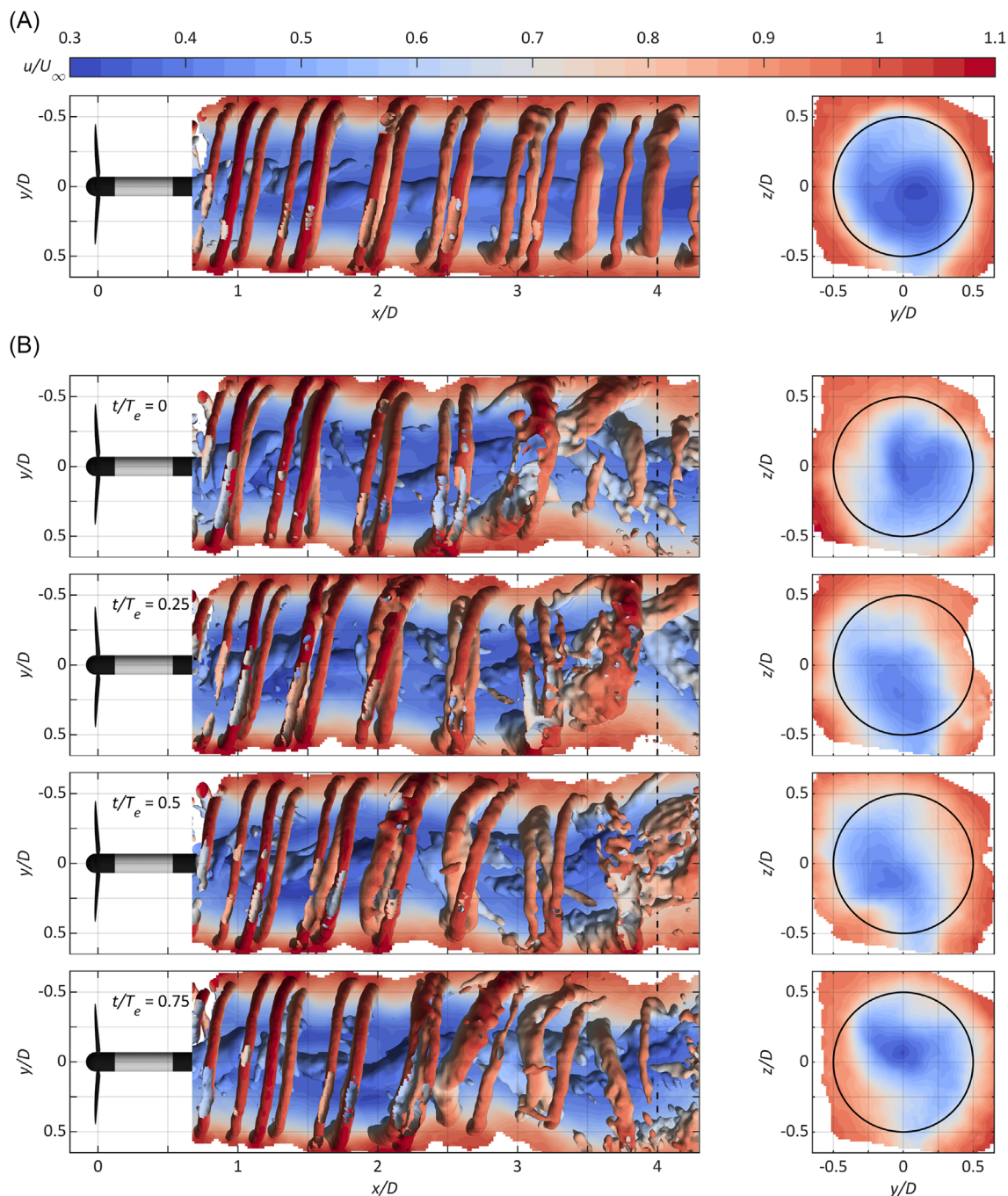


**FIGURE 9** Phase-averaged velocity contours  $u/U_\infty$  at turbine hub height ( $z/D=0$ ) and of a cross-section of the wake at  $x/D=4$ . The wake of a single rotor azimuth bin of the baseline operation case (A) is compared with multiple phases (i.e., rotor azimuth bins with corresponding helix azimuth angles as indicated in Figure 8) of the CW helix cycle (B). The bins that were nearest to the normalized time  $t/T_e$  were used to provide the flow field data for the helix case. Isosurfaces of the  $Q$ -criterion, with  $Q=30$ , visualize the tip vortices and their interaction downstream. CW, clockwise.

both start increasing at a similar rate. The variation in power level depending on the different phases in the helix actuation sequence due to the horizontal and vertical movement of the wake is also visualized by the shaded areas. The CW method was able to reach a slightly higher power level, likely as a result of the higher pitch amplitude. If we also compare it to the available power with  $CCW_{opt}$ , we see an even earlier recovery of the wake ( $x/D=1.5$ ) and higher power levels further downstream compared with the two other helix cases.

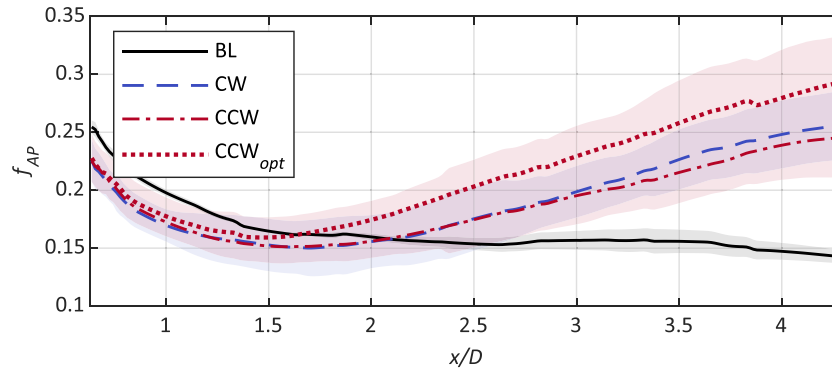


**FIGURE 10** Evolution of the fraction of available power over the downstream distance  $x/D$ . The  $f_{AP}$  is based on the power extracted by a hypothetical turbine rotor using the phase-averaged velocity fields. The shaded areas indicate the variation in power levels over the different phase bins, expressed by  $\pm 2\sigma$

### 3.3 | Kinetic energy entrainment

Next, we consider the phase-averaged entrainment into the wake due to shear stresses caused by random fluctuations. This process has been identified as the dominant factor for re-energizing the wake, following the tip vortex breakdown<sup>42</sup>. The phase-averaged Reynolds stress in the vertical plane for a single phase  $\phi$  is defined as

$$\langle u_s w_s \rangle_\phi = \frac{\sum_{k=1}^N (u(t_{k,\phi}) - \langle u \rangle_\phi) (w(t_{k,\phi}) - \langle w \rangle_\phi)}{N}, \quad (9)$$

with  $\langle u \rangle_\phi$  and  $\langle w \rangle_\phi$  the phase-averaged in-plane velocity components and  $t_{k,\phi}$  the sampling time for a velocity component in phase bin  $\phi$ . In this case, the periodic fluctuations are now an inherent part of the phase-averaged velocity  $\langle u \rangle_\phi$ . However, the phase-averaging procedure adopted in this paper did not result in strictly phase-locked measurements, as the phase bins contain a collection of smaller phases.

Multiple phases of the phase-averaged shear stress are visualized in Figure 11. The dashed line indicates the edge of the wake, meaning that any red areas crossing this line represent a positive flux of kinetic energy into the wake. The solid black line in the figure indicates the streamwise velocity contour of  $\langle u \rangle / U_\infty = 0.5$ . The flow from the baseline case shows how saddle points mark the location of subsequent tip vortices. Furthermore, the initial onset of two pairing vortices can be observed just before  $x/D = 1.5$ . Judging from the sign flip of the shear stress a little further downstream, the leapfrogging motion has just been completed for another pair of vortices at that location. Moving further downstream, we now see more positive contributions of the shear stress crossing over into the turbine wake. The second part of Figure 11 shows the phase-averaged Reynolds stress at different phases of the CCW helix cycle, which are marked by the location of the resultant tilt and yaw angles. Considering the first phase that is presented, we initially also see some saddle points indicating the presence of tip vortices. The shear stress quickly becomes more dominant compared with the baseline case as we move further downstream, concentrating in a larger area around  $x/D = 2.5$ . Moving on to the next frames in the helix cycle, we can observe how more energy is accumulated as the flow moves downstream, and subsequently passes the wake boundary. This area of concentrated shear stress is seen to coincide with a local shifting of the wake, which is marked by the velocity contour.

Figure 11 illustrated how the entrainment of kinetic energy as shown by the phase-averaged Reynolds stress varied over different phases of the helix cycle. By averaging these results over all considered phases, we can obtain an expression for the net entrainment of kinetic energy into the wake as a result of random turbulent motions in the flow. The average Reynolds stress due to random fluctuations over all phases is given by

$$\overline{u_s w_s} = \sum_{\phi=1}^{N_f} \frac{\langle u_s w_s \rangle_\phi}{N_f} \quad (10)$$

for a number of phases  $N_f$ . Multiplying this term with the time-averaged velocity provides the flux of mean kinetic energy due to random fluctuations:

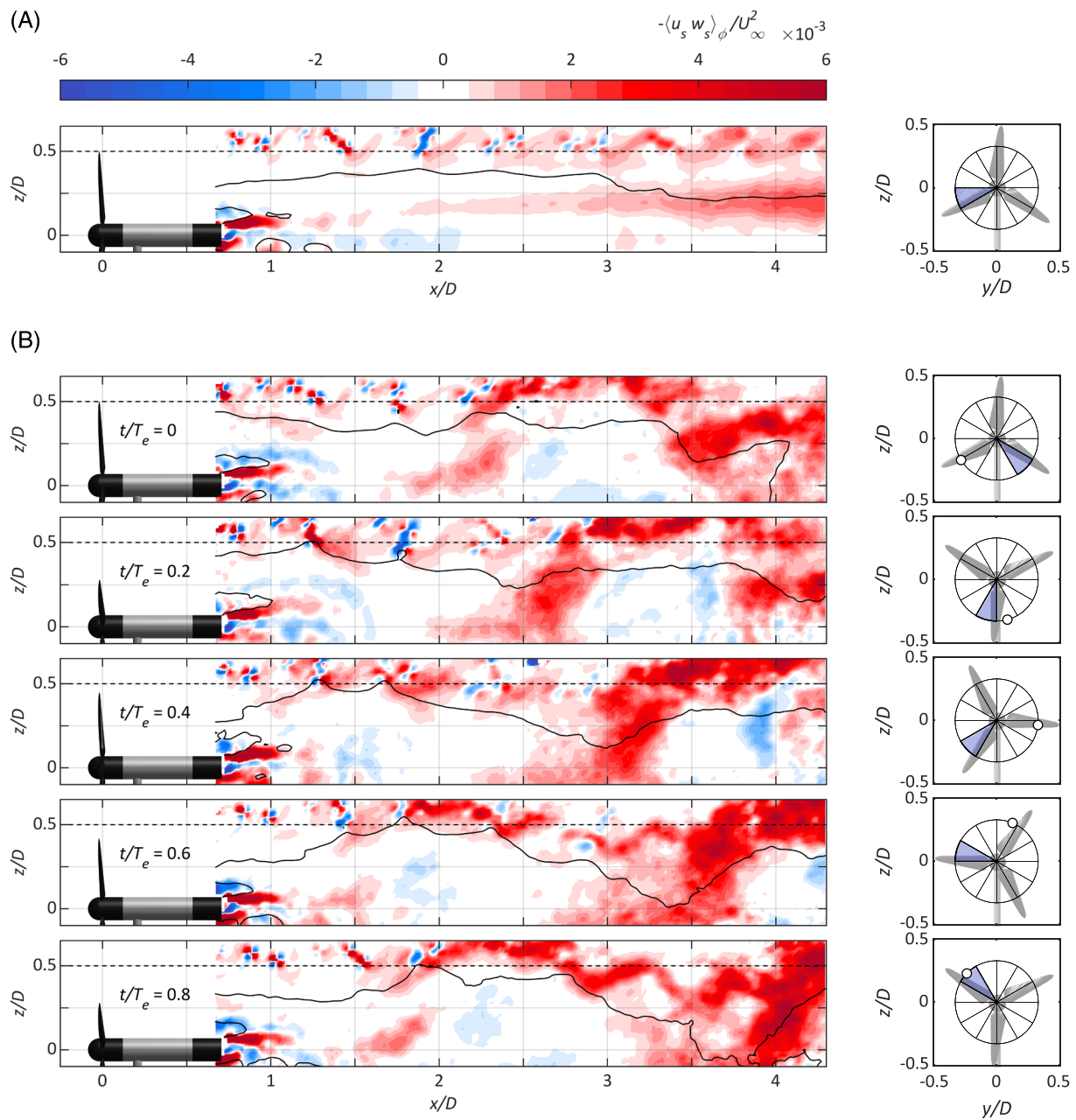


**FIGURE 11** Phase-averaged Reynolds stress in the vertical plane ( $y/D = 0$ ) for baseline operation (a) and the CCW helix approach (b). Positive (red) values indicate flux of mean kinetic energy in the negative  $z$  direction (downward). We are mostly interested in the energy that crosses the border of the wake shown by the dashed black line. The solid black contour line indicates a streamwise velocity of  $\langle u \rangle_\phi / U_\infty = 0.5$ . The phase bins that were nearest to the normalized time  $t/T_e$  were used to provide the flow field data for the helix case. The different phases of the helix approach are illustrated on the right-hand side by the location of the resultant tilt and yaw moment over the rotor plane. The corresponding rotor azimuth bin is indicated by the blue shaded area.

$$\Phi_s = -\overline{u_s w_s \bar{u}}. \quad (11)$$

Figure 12 presents the mean transport of kinetic energy into the wake as a result of random fluctuations for the three considered test cases. Comparing the baseline result to the one from Figure 7, we no longer observe a sign flip in the flux. This area marked the leapfrogging location, which was dominated by periodic fluctuations resulting from the tip vortices. These periodic fluctuations do not have a positive net contribution to the recovery of the wake<sup>42</sup>. This is confirmed by Figure 12, which shows that the entrainment is dominated by the region after the leapfrogging occurrence. Both implementations of the helix approach show a clear increase in the kinetic energy flux. The helix is able to achieve higher levels of mean kinetic energy flux due to the meandering movement of the wake. Furthermore, the entrainment starts at a shorter distance from the rotor plane. We believe this to be the result of enhanced interaction between tip vortices, which will be considered in the next section.

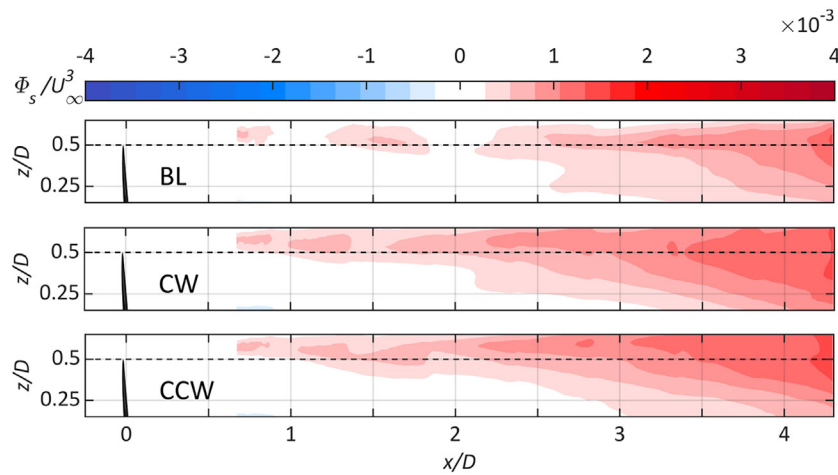


**FIGURE 12** Vertical flow field ( $y/D=0$ ) of the normalized flux of mean kinetic energy due to random fluctuations into the wake region. Positive (red) values indicate flux of mean kinetic energy in the negative  $z$  direction (downward). We are primarily interested in the flux crossing the boundary of the wake, marked by the dashed line. The figure shows a comparison between baseline operation, CW helix, and CCW helix. CW, clockwise; CCW, counter-clockwise.

### 3.4 | Tip vortex evolution

The effect of the tip vortex instability on the recovery of the wake has been mentioned several times before in this paper. Using simulations with a vortex-particle-mesh code, Coquelet<sup>38</sup> showed how the meandering of the wake was triggered differently depending on the resolution of the simulations. At low to intermediate resolution, the wake was destabilized by Kelvin-Helmholtz instabilities, resulting in a meandering wake. When a sufficiently high resolution was used to fully resolve the tip vortices, the manner of destabilization changed to vortex pairing induced instabilities. The phase-averaged PIV flow fields also provide a good opportunity to study how the helix implementation affects the tip vortex pairing and initializes the destabilization of the wake.

The evolution of the tip vortices is compared for the baseline and CCW helix case in Figure 13 using the three-dimensional vorticity magnitude  $|\omega| = \sqrt{\omega_x^2 + \omega_y^2 + \omega_z^2}$ , with  $\omega_x = \frac{\partial w}{\partial y} - \frac{\partial v}{\partial z}$ , and  $\omega_y$  and  $\omega_z$  similarly defined. For each test case, the tip vortices were tracked over time using a least-squares estimate of the displacement  $\delta$  in  $x$  and  $y$  directions, based on two consecutive vorticity flow fields. To account for any rotation of the vortices that could not be properly estimated, the least-squares estimates were subsequently corrected with a local peak-finding algorithm. The peak location of the vorticity magnitude was taken as the center of each vortex. For every consecutive phase bin, the positions of each vortex center along with the corresponding magnitude were recorded. Due to the quasi-steady nature of the baseline wake, only a single set of tip vortices needed to be tracked. For the helix cases, a set of vortices was tracked after the completion of each rotor revolution.

When operating the turbine using baseline control, Figure 13 shows a very clear evolution of the tip vortices as they convect downstream. At around  $x/D=1.75$ , one can observe the leapfrogging of the first vortex pair. The first vortex is subsequently passed by the last trailing vortex, which completes the leapfrogging of the second vortex around  $x/D=3$ . While the vortices are seen to interact with each other, there is no clear sign of any instability yet with all the vortices staying more or less intact. The vorticity plots of the CCW helix case show one of the sets that experience the most aggressive mutual inductance. The leapfrogging of the first vortex pair has already taken place before  $x/D=1.5$ , which is earlier compared with the baseline case. Comparing the last frame of the two cases, we see that the third vortex has already jumped the first two vortices. On further inspection, we can also notice that the set of vortices has convected less far downstream. This also shows how the helix influences the convection velocity of the vortices over time, which in turn causes sets of vortices to expand outward or contract toward the center of the wake. All previously mentioned phenomena are seen to destabilize the wake at a very fast rate.

One of the responsible factors for the higher mutual inductance of the tip vortices is the strength of the vortices (i.e., stronger vortices will have a larger relative influence and thus increased interaction). By tracking all sets of vortices over time, we can also see how the strength of each vortex evolves over time (and distance downstream). Figure 14 presents the average vorticity magnitude of each trailing vortex as it travels downstream. The resulting plots were obtained by fitting a third-order polynomial on all of the recorded vortex measurements. It is seen how the vorticity magnitude of both helix implementations is initially higher than the baseline case, leading to a stronger interaction initially. However, after the initial interaction between vortices, we observe that the magnitude decreases at a faster rate for the helix. Considering the magnitude of the third vortex, we see a striking difference compared with the first two vortices. For all three test cases, the initial vorticity is almost twice as low compared with the first and second vortices. Although the exact reason behind this difference is unknown, we reckon this is either the result of a slight offset in the pitch angle of one of the blades, or imperfections on the blade surface near the tip.

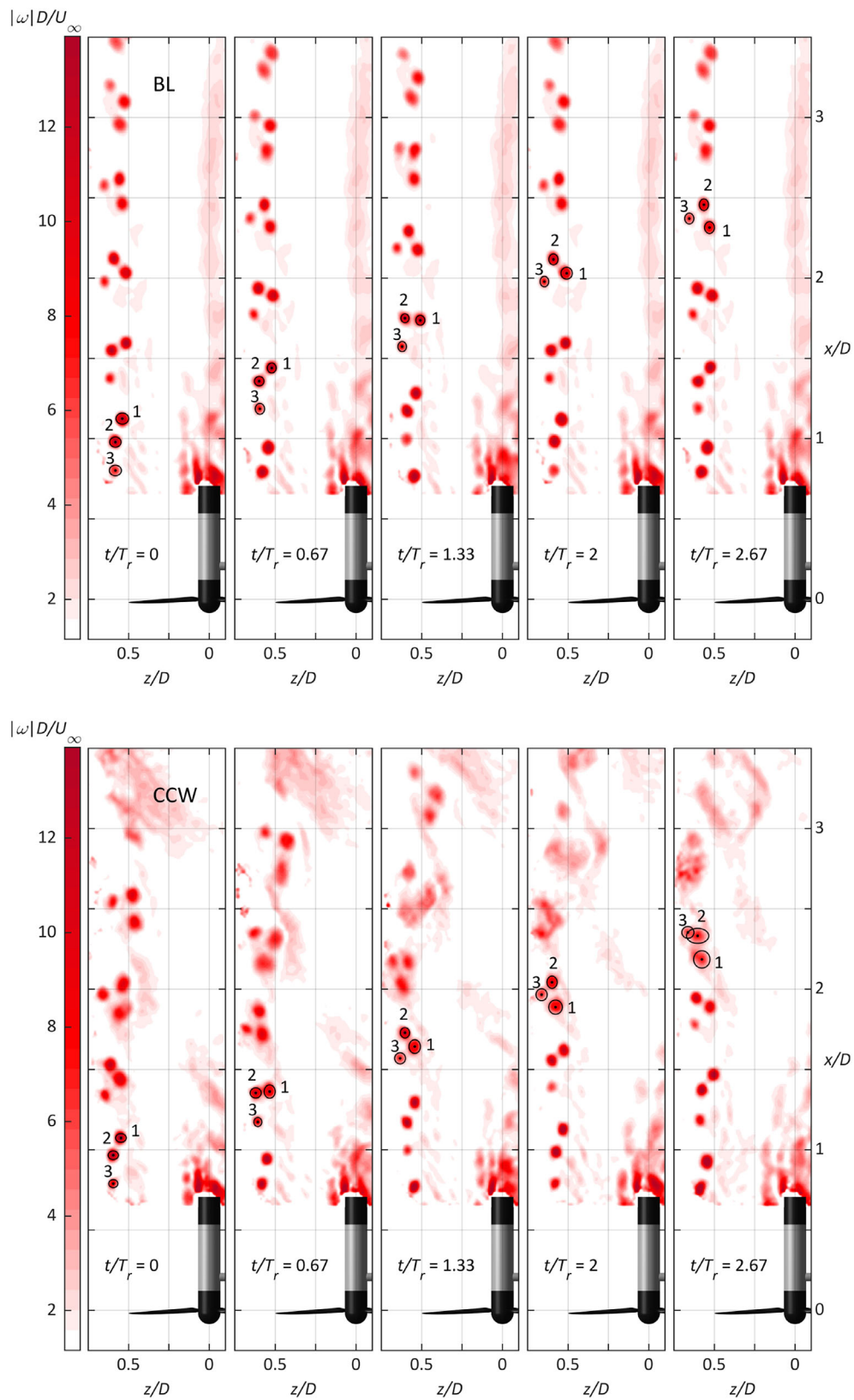


**FIGURE 13** Evolution of the tip vortices, expressed by the normalized vorticity magnitude  $|\omega|D/U_\infty$ , as they travel downstream. The vorticity fields were reconstructed from the phase-averaged measurement data. The figure compares the interaction between the tip vortices for several phases, in the case of baseline operation (top) and the CCW helix approach (bottom). For the helix approach, the vorticity fields also correspond to phases  $t/T_e = \{0, 0.12, 0.24, 0.35, 0.47\}$ . CCW, counter-clockwise.



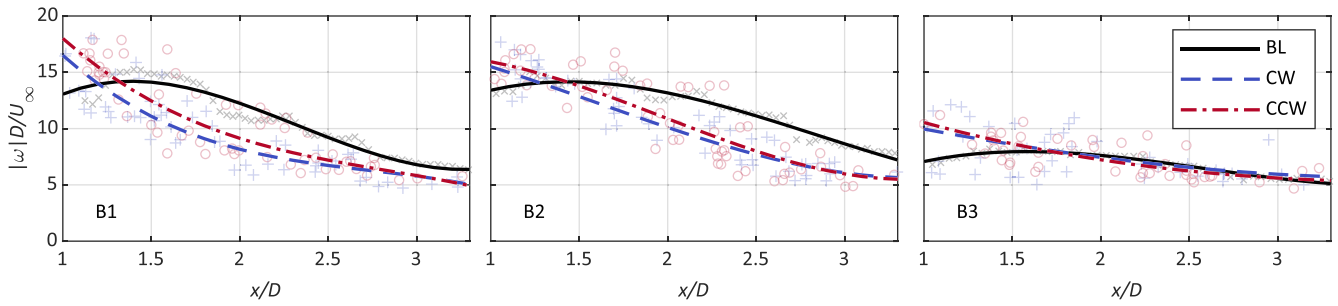


**FIGURE 14** Vortex strength expressed by the normalized vorticity magnitude as a function of the displacement in the streamwise direction for three different test cases based on the phase-averaged vorticity fields. Each figure corresponds to a vortex shed by one of the blades. The measurements were fitted to a third-order polynomial to obtain the average vorticity magnitude for each test case. A subset of the measurements to which the polynomials were fitted is included for the baseline ( $\times$ ), CW ( $+$ ), and CCW ( $\circ$ ) cases. CW, clockwise; CCW, counter-clockwise.

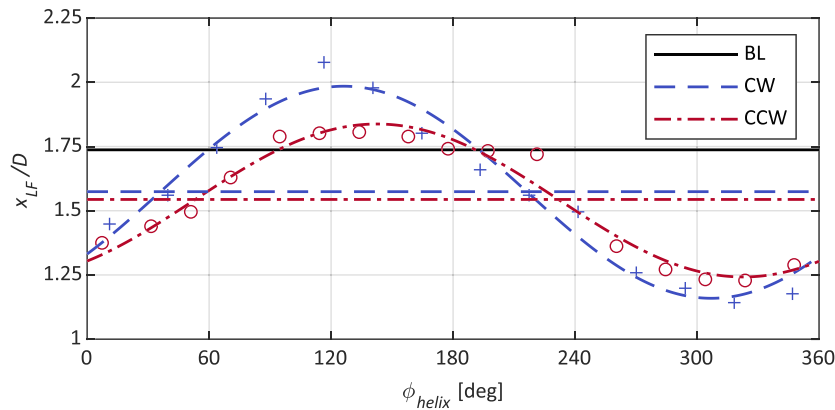


**FIGURE 15** Comparison of the leapfrogging location  $x_{LF}/D$  in the vertical plane ( $y/D=0$ ) as a function of the helix azimuth  $\phi_{helix}$ , which is a measure of the position of the combined yaw and tilt moment on the rotor plane. The figure was created using the phase-averaged vorticity fields. A constant  $x_{LF}/D$  is shown for the baseline case, while the varying locations for the helix approach are marked by  $+$  and  $\circ$  for the CW and CCW cases, respectively. These data points were subsequently fitted to a sine function of the form  $a_1 + a_2 \sin(a_3 t + a_4)$ , with average offset  $a_1$ , amplitude  $a_2$ , frequency  $a_3$  and phase offset  $a_4$ . The average leapfrogging locations for the CW and CCW cases are indicated by the horizontal lines in matching line styles. CW, clockwise; CCW, counter-clockwise.

The tracking measurements also allow us to express the variation in the leapfrogging location of the first vortex pair as a function of the helix azimuth  $\phi_{helix}$ . For each of the vortex pairs, this location was marked when the second vortex moves over  $90^\circ$  with respect to the first vortex (i.e.,  $x_{v_2}(\phi) > x_{v_1}(\phi)$ , with  $x_{v_i}$  indicating the streamwise location of a vortex  $i$  for phase  $\phi$ ). The  $90^\circ$  rotation was identified by Lignarolo et al<sup>42</sup> as the wake location that preceded a rapid increase in kinetic energy flux. The resulting locations are presented in Figure 15 and compared with the constant leapfrogging location of the baseline case. The respective data points were subsequently fitted to a sine function, which shows how the pairing of the first two vortices evolves as the resultant yaw and tilt moment moves around the rotor plane. It appears that the CW helix has a slightly higher amplitude than the CCW case, probably related to the difference in pitch amplitude between the two cases. Furthermore, we show that on average the helix implementation initializes the leapfrogging at an earlier stage.

### 3.5 | Turbine measurements

Besides analyzing the performance of the helix approach based on the flow fields, a more straightforward approach is to investigate the measurements of the turbines themselves. During each PIV recording, the generator power and bending moment at the tower bottom were measured. For each test case, all these measurements were processed to obtain the average and standard deviations. Since each PIV measurement was triggered at the same time instant with respect to the rotor azimuth angle and helix actuation, the periodic components in the generator power and bending moment were maintained, at least for turbine T1.

Figure 16 provides the bending moments of both turbines. The periodic excitation of the tilt moment initiated by the helix approach is visible at T1, especially for the CCW helix cases. For all helix cases, the average bending moment experienced at the base of the tower increased. In the case of an ideal implementation of the helix approach, the collective blade pitch angle should remain the same as in the baseline case, and hence a similar average bending moment is expected. The increase in bending moment that we observe at the upstream turbine is possibly the result of the imperfect blade pitch actuation by the swashplate. The bending moment of the second turbine shows a similar response. Again, the CCW helix especially shows the effect of the periodic tilt moment very clearly. While the average bending moment experienced by the downstream turbine is smaller compared with the first turbine, the relative increase is more severe for the second turbine due to the enhanced wind speed.

The average generator power coefficients of both turbines are shown in Figure 17 for all test cases. The shaded areas represent the 95% confidence intervals of the measurement variance. We observe that the baseline case is operating at the expected power level, while a significant decrease in power is observed for each helix case. The largest drops in power are seen for the CW and CCW<sub>opt</sub> cases, which have similar pitching amplitudes of 2.5° and 2.4°, respectively. Measurements from the second turbine show that the helix approach is able to increase the power downstream by a large amount. In all cases, the original amount of power from the baseline case is more than doubled. As expected, the largest increase in power at T2 is observed for the Helix CCW<sub>opt</sub> case. Both Figures 16 and 17 make it apparent, that while large gains in power are possible with the helix implementation, this will come at the cost of increased fatigue loading of some structural components. Another observation is the periodic component present in all power measurements of T1. A closer inspection of the signal showed this as a 2P excitation, meaning it corresponds to two times the rotational frequency of the turbine. This 2P excitation in the fixed frame can be caused by an offset in the pitch angle of one of the blades.<sup>56</sup> This was already speculated on in the previous section when observing the vorticity magnitude of one of the tip vortices.

Finally, the performance of maximizing the power output for all considered test cases is summarized in Figure 18. The figure presents the average power generated by each turbine, as well as the combined power of T1 and T2. Due to the periodic pitching of the blades, T1 loses some aerodynamic efficiency, decreasing the power by more than 10% for each implementation of the helix approach. Compared with previously reported power losses from simulation studies that were in the range of 1%–5%<sup>31,33,34,38</sup>, these decreases are quite severe. This is primarily due to the relatively high sensitivity of the MoWiTO's steady-state power coefficient to changes in pitch angle. The largest drop in power is observed for the CCW<sub>opt</sub> helix, indicating that the loss in performance can not only be ascribed to the pitch amplitude. Further study is required to find out what else is responsible for the increased performance losses. The power of the second turbine was seen to double for the first two helix

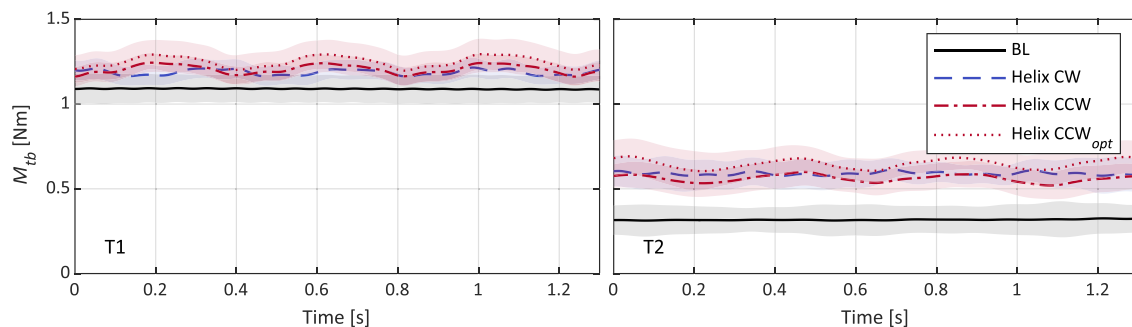


**FIGURE 16** Sample of the average measured bending moment at the tower base of turbines T1 and T2. Some variation between different measurements of the same test case was observed. This variation is given by the shaded areas around the mean, indicating  $\pm 2\sigma$

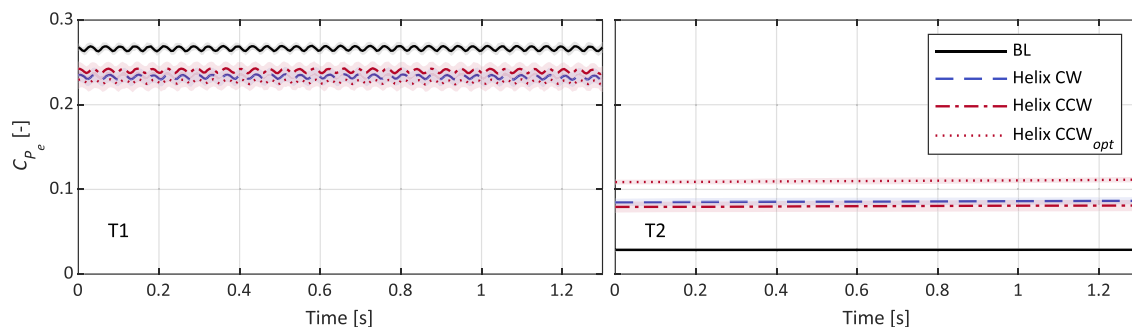


**FIGURE 17** Sample of the average measured generator power coefficient of turbines T1 and T2. For both turbines, the power coefficient was determined with respect to the free stream velocity  $U_\infty = 5 \text{ m s}^{-1}$ . Some variation between different measurements of the same test case was observed. This variation is given by the shaded areas around the mean, indicating  $\pm 2\sigma$

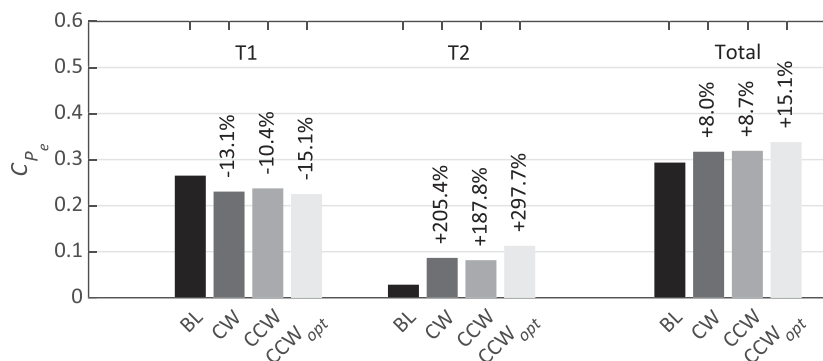


**FIGURE 18** Average power production of turbines T1, T2, and the combined sum of both turbines for the different control strategies expressed by the electrical power coefficient  $C_{p_e}$ . The power coefficients of both turbines were determined with respect to the free stream inflow velocity  $U_\infty = 5\text{ms}^{-1}$ . The total power coefficient is the sum of these two values.

approaches, and even triple for the  $\text{CCW}_{\text{opt}}$  helix. Adding up the power of both turbines, we observe that for this particular setup (5D spacing with low turbulence), the helix approach was able to increase power by 8.0% for the CW direction, by 8.7% for the CCW direction, and by 15.1% using the  $\text{CCW}_{\text{opt}}$  helix with higher pitch amplitude. Based on the work of Taschner et al,<sup>34</sup> we believe even higher gains could be achieved when larger pitch amplitudes are applied in combination with the CCW helix. However, when one considers higher levels of atmospheric turbulence, the performance of the helix approach decreases due to the enhanced wake recovery in the baseline case that is associated with increased turbulence.<sup>35</sup>

## 4 | CONCLUSIONS

This paper presented the implementation of the *helix approach*, a promising control method for maximizing the power output of a wind farm, in a wind tunnel study. The experimental setup consisted of two scaled wind turbines ( $D = 0.58\text{m}$ ) spaced  $5D$  apart in front of an open jet. The upstream turbine was modified with a swashplate typically used for helicopter controls, allowing the turbine to mimic DIPC. A tomographic particle image velocimetry setup, using HFSBs as flow tracers, was used to measure the effect of the helix approach on the turbine wake. A comparison was made with a baseline case, which consisted of running the first turbine at the optimal power extraction settings (greedy control). Turbine measurements of the generator power and tower bending moment were collected as well.

The helix approach uses DIPC to create yaw and tilt moments from the rotor plane that are acting on the incoming flow. The resultant moment is then periodically moved over the rotor plane, resulting in a helical velocity profile in the wake. Two types of implementation are possible with the helix, either moving the helical velocity profile in a CW or CCW direction. Previous work on the helix approach was mostly limited to simulation studies. This paper contributes to the experimental validation of the control method, which in time may lead to the implementation of this method in the field. Using phase-averaged measurements of the streamwise velocity component, the amount of available power in the wake was determined for all test cases. All helix implementations that were considered showed an earlier and enhanced recovery of the wake, providing more energy for turbines downstream.

Phase-averaged flow fields were also used to investigate the wake recovery mechanism in further detail. Previous studies on the helix approach, as well as DIC with collective pitch, indicated that the performance of the control framework is related to the leapfrogging or vortex pairing instability of the shed tip vortices. It has been shown that this pairing initializes the breakdown of the tip vortices and is the onset of the re-energization of the wake. The periodic motion of the combined yaw and tilt moment results in tip vortices varying in strength and size, as well as the low-velocity wake being moved in a circular motion. Therefore, the mutual inductance between vortices will also differ depending on time and place. Overall, it is believed these local variations will trigger the breakdown of vortices and destabilization of the wake, which will subsequently result in a forced meandering of the wake. The phase-averaged measurements showed a clear increase in the entrainment of kinetic energy in the wake due to random fluctuations. Furthermore, after tracking the tip vortices over time using the vorticity magnitude, we showed that the average leapfrogging location of the first vortex pair is shortened with the helix approach.

Finally, measurements from both turbines were used to corroborate the enhanced performance of the helix approach compared with normal operation that was obtained through the flow measurements. The turbine that was used to implement the helix approach did suffer from a loss in aerodynamic efficiency, leading to decreases in power of over 10%. However, these losses were more than made up for by the downstream turbine, enhancing the total power output of the two turbines by as much as 15%. These results are even more promising when one considers that, according to high-fidelity simulation studies, the losses at the first turbine are expected to decrease in the case of utility-scale wind turbines. The measurement results also confirm once more that the CCW helix is the more effective of the two implementations.

## ACKNOWLEDGMENTS

This work is part of the Hollandse Kust Noord wind farm innovation program where CrossWind C.V., Shell, Eneco, and Siemens Gamesa are teaming up; funding for the PhDs was provided by CrossWind C.V. and Siemens Gamesa. We would like to extend great thanks to Will van Geest, Wim Wien, and the people from DEMO at TU Delft for their support in preparing the scaled wind turbine models.

## CONFLICT OF INTEREST STATEMENT

Carlos Simão Ferreira is one of the editors for Wind Energy.

## PEER REVIEW

The peer review history for this article is available at <https://www.webofscience.com/api/gateway/wos/peer-review/10.1002/we.2896>.

## DATA AVAILABILITY STATEMENT

The experimental data that were presented in this paper has been uploaded to the 4TU research data base under doi 10.4121/22294423.v1.

## SUPPORTING INFORMATION

The experimental data that were presented in this paper has been uploaded to the 4TU research database under doi 10.4121/22294423.

## ORCID

Daan van der Hoek  <https://orcid.org/0000-0002-8781-5661>

Jan-Willem van Wingerden  <https://orcid.org/0000-0003-3061-7442>

## REFERENCES

1. Barthelmie RJ, Hansen K, Frandsen ST, Rathmann O, Schlez W, Phillips J, Hassan G, Rados UK, Zervos A. Modelling and measuring flow and wind turbine wakes in large wind farms offshore. *Wind Energy*. 2009;12:431-444.
2. Barthelmie RJ, Hansen KS, Pryor SC. Meteorological controls on wind turbine wakes. *Proc IEEE*. 2013;101(4):1010-1019.
3. van Wingerden JW, Fleming PA, Göçmen T, et al. Expert elicitation on wind farm control. *J Phys: Confer Ser*. 2020;1618(2):022025.
4. Meyers J, Bottasso C, Dykes K, Fleming P, Gebraad P, Giebel G, Göçmen T, van Wingerden JW. Wind farm flow control: Prospects and challenges. *Wind Energy Sci*. 2022;7(6):2271-2306.
5. Houck DR. Review of wake management techniques for wind turbines. *Wind Energy*. 2022;25(2):195-220.
6. Kanev SK, Savenije FJ, Engels WP. Active wake control: An approach to optimize the lifetime operation of wind farms. *Wind Energy*. 2018;21(7):488-501.
7. Aho J, Buckspan A, Laks J, Fleming PA, Jeong Y, Dunne F, Churchfield M, Pao LY, Johnson K. A tutorial of wind turbine control for supporting grid frequency through active power control. In: American Control Conference (ACC); 2012:3120-3131.
8. Fleming PA, Aho J, Gebraad PMO, Pao LY, Zhang Y. Computational fluid dynamics simulation study of active power control in wind plants. In: American Control Conference (ACC); 2016:1413-1420.
9. Vali M, Petrović V, Boersma S, Van Wingerden JW, Kühn M. Adjoint-based model predictive control of wind farms: Beyond the quasi steady-state power maximization. *IFAC World Congr*. 2017;50(1):4510-4515.
10. Fleming PA, Aho J, Buckspan A, Ela E, Zhang Y, Gevorgian V, Scholbrock A, Pao L, Damiani R. Effects of power reserve control on wind turbine structural loading. *Wind Energy*. 2016;19(3):453-469.
11. van der Hoek D, Kanev S, Engels W. Comparison of down-regulation strategies for wind farm control and their effects on fatigue loads. In: Proceedings of the American Control Conference, Vol. 2018-June; 2018.
12. Annoni J, Gebraad PMO, Scholbrock AK, Fleming PA, van Wingerden JW. Analysis of axial-induction-based wind plant control using an engineering and a high-order wind plant model. *Wind Energy*. 2016;19(6):1135-1150.
13. Campagnolo F, Petrovie V, Bottasso CL, Croce A. Wind tunnel testing of wake control strategies. In: Proceedings of the American Control Conference (ACC); 2016:513-518.
14. van der Hoek D, Kanev S, Allin J, Bieniek D, Mittelmeier N. Effects of axial induction control on wind farm energy production—a field test. *Renew Energy*. 2019;140:994-1003.
15. Frederik JA, Weber R, Cacciola S, Campagnolo F, Croce A, Bottasso C, van Wingerden JW. Periodic dynamic induction control of wind farms: proving the potential in simulations and wind tunnel experiments. *Wind Energy Sci*. 2020;5(1):245-257.
16. Gebraad PMO, Teeuwisse FW, van Wingerden JW, Fleming PA, Ruben SD, Marden JR, Pao LY. Wind plant power optimization through yaw control using a parametric model for wake effects - a CFD simulation study. *Wind Energy*. 2016;19(1):95-114.
17. Fleming PA, Annoni J, Scholbrock AK, Quon E, Dana S, Schreck S, Raach S, Haizmann F, Schlipf D. Full-scale field test of wake steering. *J Phys: Confer Ser*. 2017;854(1):012013.
18. Fleming P, King J, Dykes K, et al. Initial results from a field campaign of wake steering applied at a commercial wind farm: part 1. *Wind Energy Sci Discuss*. 2019;2019:1-22.
19. Fleming P, Sinner M, Young T, Lannic M, King J, Simley E, Doekemeijer B. Experimental results of wake steering using fixed angles. *Wind Energy Sci*. 2021;6(6):1521-1531.
20. Howland MF, Lele SK, Dabiri JO. Wind farm power optimization through wake steering. *Proc Natl Acad Sci*. 2019;116(29):14495-14500.
21. Howland MF, Bas Quesada J, José Pena Martínez J, Palou Larrañaga F, Yadav N, Chawla JS, Sivaram V, Dabiri JO. Collective wind farm operation based on a predictive model increases utility-scale energy production. *Nature Energy*. 2022;7(9):818-827.

22. Doekemeijer BM, Kern S, Maturu S, et al. Field experiment for open-loop yaw-based wake steering at a commercial onshore wind farm in Italy. *Wind Energy Sci.* 2021;6(1):159-176.
23. Goit JP, Meyers J. Optimal control of energy extraction in wind-farm boundary layers. *J Fluid Mech.* 2015;768:5-50.
24. Munters W, Meyers J. An optimal control framework for dynamic induction control of wind farms and their interaction with the atmospheric boundary layer. *Phil Trans R Soc London A: Math, Phys Eng Sci.* 2017;375(2091):20160100.
25. Munters W, Meyers J. Towards practical dynamic induction control of wind farms: analysis of optimally controlled wind-farm boundary layers and sinusoidal induction control of first-row turbines. *Wind Energy Sci.* 2018;3(1):409-425.
26. Yilmaz AE, Meyers J. Optimal dynamic induction control of a pair of inline wind turbines. *Phys Fluids.* 2018;30(8):085106.
27. Brown K, Houck D, Maniaci D, Westergaard C, Kelley C. Accelerated wind-turbine wake recovery through actuation of the tip-vortex instability. *AIAA J.* 2022;60(5):3298-3310.
28. Croce A, Cacciola S, Montero Montenegro M, Stipa S, Praticó R. A CFD based analysis of dynamic induction techniques for wind farm control applications. *Wind Energy.* 2023;26(3):325-343.
29. van der Hoek D, Frederik J, Huang M, Scarano F, Simao Ferreira C, van Wingerden JW. Experimental analysis of the effect of dynamic induction control on a wind turbine wake. *Wind Energy Sci.* 2022;7(3):1305-1320.
30. Lignarolo LEM, Ragni D, Krishnaswami C, Chen Q, Simão Ferreira CJ, van Bussel GJW. Experimental analysis of the wake of a horizontal-axis wind-turbine model. *Renew Energy.* 2014;70:31-46.
31. Frederik JA, Doekemeijer BM, Mulders SP, van Wingerden JW. The helix approach: using dynamic individual pitch control to enhance wake mixing in wind farms. *Wind Energy.* 2020;23:1739-1751.
32. Muscari C, Schito P, Viré A, Zasso A, van der Hoek D, van Wingerden JW. Physics informed DMD for periodic dynamic induction control of wind farms. *J Phys: Confer Ser.* 2022;2265(2):022057.
33. Korb H, Asmuth H, Stender M, Ivanell S. Exploring the application of reinforcement learning to wind farm control. *J Phys: Confer Ser.* 2021;1934(1):012022.
34. Taschner E, van Vondelen AAW, Verzijlbergh R, van Wingerden JW. On the performance of the helix wind farm control approach in the conventionally neutral atmospheric boundary layer. *J Phys: Confer Ser.* 2023;2505:12006.
35. Korb H, Asmuth H, Ivanell S. The characteristics of helically deflected wind turbine wakes. *J Fluid Mech.* 2023;965:A2.
36. Frederik JA, van Wingerden JW. On the load impact of dynamic wind farm wake mixing strategies. *Renew Energy.* 2022;194:582-595.
37. van Vondelen AAW, Navalkar ST, Kerssemakers DRH, van Wingerden JW. Enhanced wake mixing in wind farms using the Helix approach: a loads sensitivity study. In: 2023 American Control Conference (ACC); 2023:831-836.
38. Coquelet M. Numerical investigation of wind turbine control schemes for load alleviation and wake effects mitigation. *Ph.D. Thesis: Université catholique de Louvain*; 2022.
39. Heckmeier FM. Multi-hole probes for unsteady aerodynamics analysis. *Ph.D. Thesis: Technische Universität München*; 2022.
40. Cal RB, Lebrón J, Castillo L, Kang HS, Meneveau C. Experimental study of the horizontally averaged flow structure in a model wind-turbine array boundary layer. *J Renew Sustain Energy.* 2010;2(1):013106.
41. Rockel S, Camp E, Schmidt J, Peinke J, Cal R, Hölling M. Experimental study on influence of pitch motion on the wake of a floating wind turbine model. *Energies.* 2014;7(4):1954-1985.
42. Lignarolo LEM, Ragni D, Scarano F, Simão Ferreira CJ, van Bussel GJW. Tip-vortex instability and turbulent mixing in wind-turbine wakes. *J Fluid Mech.* 2015;781:467-493.
43. Schottler J, Hölling A, Peinke J, Hölling M. Design and implementation of a controllable model wind turbine for experimental studies. *J Phys: Confer Ser.* 2016;753(7):072030.
44. Bossanyi EA. The design of closed loop controllers for wind turbines. *Wind Energy.* 2000;3(3):149-163.
45. Bir G. Multi-blade coordinate transformation and its application to wind turbine analysis. 46th AIAA Aerospace Sciences Meeting and Exhibit; 2008.
46. Scarano F, Ghaemi S, Caridi GCA, Bosbach J, Dierksheide U, Sciacchitano A. On the use of helium-filled soap bubbles for large-scale tomographic PIV in wind tunnel experiments. *Exper Fluids.* 2015;56(2):1-12.
47. Sciacchitano A, Scarano F. Elimination of PIV light reflections via a temporal high pass filter. *Meas Sci Technol.* 2014;25(8):084009.
48. Wieneke B. Volume self-calibration for 3D particle image velocimetry. *Exper Fluids.* 2008;45(4):549-556.
49. Schanz D, Gesemann S, Schröder A. Shake-The-Box: Lagrangian particle tracking at high particle image densities. *Exper Fluids.* 2016;57:70.
50. Jux C, Sciacchitano A, Schneiders JFG, Scarano F. Robotic volumetric PIV of a full-scale cyclist. *Exper Fluids.* 2018;59(4):74.
51. Reynolds WC, Hussain AKMF. The mechanics of an organized wave in turbulent shear flow. Part 3. Theoretical models and comparisons with experiments. *J Fluid Mech.* 1972;54(2):263-288.
52. Sørensen JN. Instability of helical tip vortices in rotor wakes. *J Fluid Mech.* 2011;682:1-4.
53. Hunt J, Wray A, Moin P. Eddies, streams, and convergence zones in turbulent flows. In: Proceedings of the Summer Program (Center for Turbulence Research); 1988:193-208.
54. Soto-Valle R, Cioni S, Bartholomay S, Manolesos M, Nayeri CN, Bianchini A, Paschereit CO. Vortex identification methods applied to wind turbine tip vortices. *Wind Energy Sci.* 2022;7(2):585-602.
55. Vollmer L, Steinfeld G, Heinemann D, Kühn M. Estimating the AKE deflection downstream of a wind turbine in different atmospheric stabilities: an LES study. *Wind Energy Sci.* 2016;1(2):129-141.
56. van Solingen E, van Wingerden JW. Linear individual pitch control design for two-bladed wind turbines. *Wind Energy.* 2015;18(4):677-697.

**How to cite this article:** van der Hoek D, den Abbeele BV, Simao Ferreira C, van Wingerden J-W. Maximizing wind farm power output with the helix approach: Experimental validation and wake analysis using tomographic particle image velocimetry. *Wind Energy.* 2024; 1-20. doi:10.1002/we.2896